# Critical behaviors of jamming in cyclically sheared frictional hard granular particles

Aile Sun[1], Yinqiao Wang[1], Yangrui Chen[1], Jin Shang[1], Xulai Sun[1], Jie Zheng[1], Yujie Wang[1], and Jie Zhang[*1,2]

[1] *School of Physics and Astronomy, Shanghai Jiao Tong University, Shanghai 200240, China*
[2] *Institute of Natural Sciences, Shanghai Jiao Tong University, Shanghai 200240, China*

(Dated: April 21, 2021)

In stark contrast to the jamming of frictionless hard-sphere (hard-disk if in two dimensions) packings, the critical jamming of frictional packings is much more elusive and still under intense debate. Here we show that frictional hard-disk packings self-organize near a critical jamming state when subjected to quasi-static steady-state cyclic shear, displaying scale-free fluctuations in particle velocity fields as characterized by the power spectra $E(k) \propto k^{-\alpha}$ for both longitudinal and transverse modes in wavevector space, with $\alpha \approx 2.0 \pm 0.15$, and the nearly flat spectra $E(\omega) \propto const.$ in angular frequency domain. Our findings agree quantitatively with the predictions of the Langevin-type effective medium theory of S. Henkes and coworkers with two diverging length scales associated respectively with the longitudinal and transverse modes, showing a hallmark of critical behaviors of jamming. Moreover, our findings are consistent with the conceptual framework of general isostaticity but with a key difference that the system self-organizes to a critical jamming state through a strong coupling of mechanical structure and dynamics. Our findings are important in providing microscopic mechanism in understanding the nonlocal rheologies and guide principles in developing constitutive relations of real granular materials.



Granular particles are frictional, which are different from atoms or molecules and the constitutive particles of other soft matter materials such as bubbles and emulsions. Our understanding of jamming of frictional particles, especially its critical behaviors, lags far behind that of frictionless counterpart. In past several decades, by studying packings of frictionless spherical particles, tremendous progress has been made towards understanding the critical behaviors of jamming transition, where a system changes from a liquid-like to a solid-like behavior upon increasing its packing fraction beyond some critical value [1–3], showing anomalous behaviors, including the divergence of length scales [2–7], critical behaviors of moduli and excess coordination numbers [1–3, 8, 9], plateau in density of states [1–5], floppy modes [4], the divergence of viscosity in rheology [10–15], power-law distributions of weak forces and particle gaps [2, 3, 16–20], yielding and shear jamming [21–24], and nonlocal and multi-scale nonaffine responses to perturbations [25]. Nonequilibium statistical mechanics frameworks have been proposed for volume, stress, and force-network ensembles [26–37]. Equilibrium statistical theories have also been proposed in building connections between jamming and glass transitions [17, 38]. In stark contrast, our understanding towards the jamming of frictional particle is still very limited and oftentimes controversial.

In frictionless jamming, one key concept is isostaticity, where the number of constraints equals exactly to the number of degrees of freedom at the jamming point: by Maxwell's counting, the contact number $Z_{iso}^{\mu=0} = 2d$, where $d$ is the dimension, e.g. $d = 2$ in two dimensions [2, 3]. Hence, breaking just one contact will produce a floppy mode, leading to a large-scale instability across system [4], which dictates much of the critical behaviors near jamming point [2, 3]. However, things become radically different considering the jamming of frictional spherical particles: a system is generally hyperstatic such that $d + 1 \leq Z \leq Z_{iso}^{\mu=0}$, where $Z = d + 1$ refers to the isostaticity of infinite friction coefficient, i.e. $\mu \to \infty$, as shown in Fig. 1. Due to tangential forces, the system finds enormous meta-stable new configurations in phase space, with a lot more freedom to explore configuration space: under a small perturbation, large-scale rearrangements are unnecessary. Therefore, critical jamming behaviors are generally irrelevant, and thus far elusive in experiments. Nonetheless, theoretically, a new concept of generalized isostaticity $Z_{iso}^{m}(\mu)$ has been proposed by considering fully mobilized contacts per particle in Maxwell's counting [2, 39–42]. A schematic of $Z_{iso}^{m}(\mu)$ is drawn using a solid line in Fig. 1, around which the yellow ribbon represents that $Z_{iso}^{m}(\mu)$ may well be protocol dependent. However, its critical nature is debatable: theoretical treatment even at the level of linear response proves controversial and challenging, with seemingly contradictory predictions from different modeling [2, 39–42]. Therefore, it is very perplexing for the critical behaviors of frictional jamming.

To probe potential critical jamming behaviors, we apply quasi-static oscillatory shear to drive densely packed circular granular particles into steady states with different shear-strain amplitudes. By investigating the spatial and temporal fluctuations of particle velocities, we show that critical jamming behaviors indeed emerge when system is driven into steady states: the system self-organizes into the vicinity of the generalized isostatic point– the critical jamming point of frictional hard particle systems [2, 39–42]. The velocity spectra show a robust power-law scaling with an exponent around $-2$ in spatial fluctuations and become nearly flat in temporal fluctuations. These observations are in quantitative agree-

ment with the theoretical prediction of Langevin dynamics with long-range elastic interactions of diverging correlation lengths [43]. The strong spatially correlated particle motion is also revealed from the probability distributions of velocity that are strongly non-Gaussian and collapsed onto a single master curve once properly normalized. Moreover, our findings reveal that the strong coupling between structure and dynamics is crucial in the self-organization process.

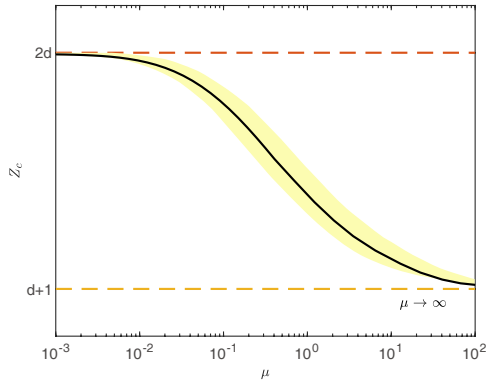


FIG. 1. The schematic of generalized isostaticity of frictional hard spherical particle packing. Here the vertical axis $Z_c$ is the mean contact number of jammed frictional hard-sphere (hard-disk if in two dimensions) packing; the horizontal axis is the friction coefficient $\mu$ in log scale. For frictional hard-sphere systems, i.e. $\mu \neq 0$, $d+1 \leq Z_c \leq 2d$, with $d$ being the dimension, e.g. $d = 2$ in two dimensions. $Z_c = 2d$, as drawn using a horizontal red dashed line, refers to the isostatic value of frictionless jamming. $Z_c = d+1$, as drawn using a horizontal orange dashed line, refers to the isostatic value of frictional jamming at the limit of $\mu \to \infty$. The general isostaticity $Z^m_{iso}(\mu)$ (discussed in details in the main text) is drawn schematically using a solid line with a yellow ribbon representing its protocol dependence.

We apply quasi-static cyclic shear to a dense horizontal layer of hard particles using a biaxial apparatus [44]. There are 2700 50 : 50 mixture of ABS cylinders of a size ratio 1.1 : 1.4. For simplicity, we will use hard disks instead of hard cylinders to refer to these particles. The ABS plastic material of our disks has a bulk modulus of $B = 2.2$ GPa and thickness of $h \sim 1$ cm, which gives a microscopic pressure per disk of $P_{mic} = Bh = 2.2 \times 10^7$ N/m. This gives, for a typical value of our applied pressure $P_0 \sim 20$ N/m, a dimensionless pressure $p = \frac{P_0}{P_{mic}} \sim 10^{-6}$. Hence, our system is indeed a hard-disk system. We take the small particle size, 1.1 cm, as the unit length. Particles are confined within a rectangular frame as shown in Fig. 2(a). In the $x$ direction, the wall positions are flexible under a constant confining force such that the packing fraction $\phi$, which is the ratio of the area of particles over the area of the rectangle, can vary. In contrast, the wall positions in the $y$ direction are controlled precisely and symmetrically by two servomotors. The shear amplitude $\gamma_m$ is the maximum strain in the $y$ direction such that within a cycle the strain $\gamma$ in the $y$ direction follows the cycle of $\gamma = 0$, $\gamma_m$, 0, $-\gamma_m$, and finally back to $\gamma = 0$ to start a new cycle. In different experiments, $\gamma_m$ can vary, with $\gamma_m = 1\%$, 2%, 3%, 4%, 5%, 8%, 10%. For each $\gamma_m$, we start cyclic shear from an initial configuration within a square frame and record images in steady-state shear cycles for several hundred cycles. The inertial number is $\sim 7 \times 10^{-6}$. Therefore, shear is quasi static. We image particle positions using two high-resolution cameras (Nikon D800), aligned, calibrated, and mounted $\sim 1.5$ m above the particle layer. We define time $t$ as the discrete number of shear cycles. For each experiment, we take multiple images within a cycle for particle tracking: to record an image, we pause shearing so particles are in mechanical equilibrium.

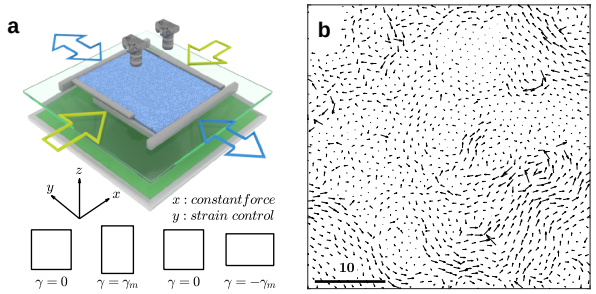


FIG. 2. (a) The schematic of experimental setup. A constant force is applied along the $x$ axis to the two boundaries of a rectangular frame. The positions of two parallel boundaries perpendicular to $y$ axis are precisely controlled by two Panasonic servomotors. The shear strain $\gamma$ is then defined as the change of size of the rectangle along $y$ axis over its initial size along the $y$ axis. Within a shear cycle, $\gamma$ varies periodically from $\gamma = 0$, to $\gamma_m$, to 0, to $-\gamma_m$, and finally back to $\gamma = 0$ to start a new shear cycle. Here $\gamma_m$ is the strain amplitude of cyclic shear. (b) One snapshot of a nonaffine particle displacement field, which is measured by tracking individual particle's position change from one shear cycle to the next shear cycle at $\gamma = 0$. The arrows are scaled up by a factor 15 for visibility. Here in this set of cyclic shear, the value of $\gamma_m$ equals 2%.

Figure2(b) shows a particle velocity field $\mathbf{v}_i$, which tracks individual particle displacement at $\gamma = 0$ between two shear cycles of $t$ and $t+1$. Interestingly, $\mathbf{v}_i$ fluctuate inhomogeneously at all scales with a strong transverse characteristic, resembling the floppy modes [4]. We can decompose $\mathbf{v}_i$ into the transverse (T) and longitudinal (L) components and compute their spectra, as discussed in detail in the Supplementary Materials (SM). Figure 3 shows that 'T' mode dominates over 'L' mode in fluctuation strength, consistent with Fig. 2(b). Both spectra $E_T(k)$ and $E_L(k) \propto k^{-\alpha}$ in the low $k$ regime with

$\alpha \approx 2 \pm 0.15$. The peaks at high $k$ are reminiscent of the static structure factor. Moreover, we also compute the spectra in the frequency domain (See SM for details), which are nearly flat with $E(\omega) \propto const.$, as shown in Fig. 4.

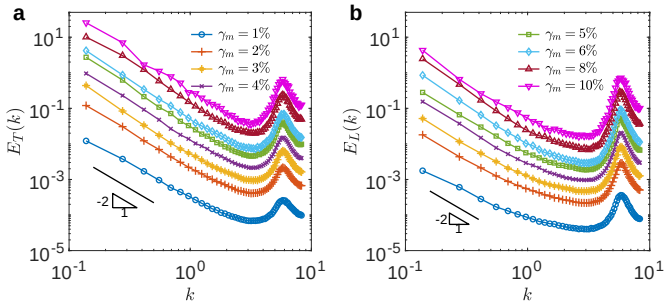


FIG. 3. The power spectra $E_T(k)$ and $E_L(k)$ of the transverse $T$ (a) and longitudinal $L$ (b) components of nonaffine displacements. Here, the wave number $k$ is scaled by the mean particle diameter $D$. For different $\gamma_m$, the spectra exhibit a power-law behavior $\propto k^{\alpha}$ with $\alpha \approx -2$.

The results in Fig. 3 and Fig. 4 can be explained using a theoretical model originally proposed to describe motion pattern of active matter [43]. There are several slightly different formulations of the model, the continuum formulation is as follows (More details can be found in SM and also in [43].

$$\zeta \dot{\mathbf{u}} = \zeta v_0 \hat{\mathbf{n}} + \bigtriangledown \cdot \hat{\sigma}, \tag{1}$$

where $\mathbf{u}$ is the displacement, $\zeta$ is a drag coefficient, the first term on the right-hand side ($r.h.s$) represents a noise term with a mean strength $v_0$ and random orientation $\hat{n}$ [43], and the second term on $r.h.s$ represents force from a continuous elastic field. For granular materials, we can think the first term on $r.h.s$ as a simplified model of the random fluctuations of contact forces due to cyclic shear and this second term on $r.h.s$ as a mean-field-type effective elastic medium [45–49]. This model predicts that the spectrum $E_T(k)$ or $E_L(k)$ shall $\propto k^{-2}$ when the transverse or longitudinal correlation length, i.e. $\xi_T$ or $\xi_L$, diverges. For practical purpose, it suffices if $\xi_{T,L} \geq \frac{L}{2}$, with $L$ referring to the system size (not the abbreviation of longitudinal mode). Meanwhile, it also predicts that $E(\omega) = const.$, if $\xi_T$ and $\xi_L$ diverge. More details can be found in Ref.[43] and SM. The long-range correlated nature of motion is also consistent with the PDFs of velocity, collapsed onto a single non-Gaussian curve once properly normalized, as shown in SFig.1 in SM.

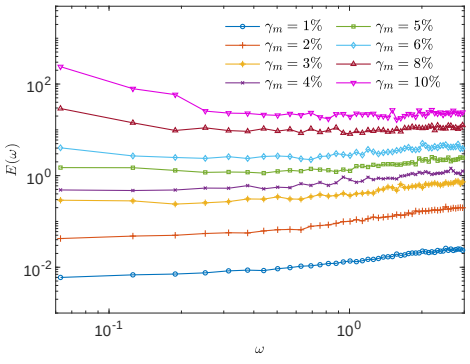


FIG. 4. Velocity power spectra $E(\omega)$ in frequency domain.

The results in Fig. 3 and Fig. 4 and their agreement with the theory suggest that the system is self-organized into a critical jamming state, which resembles the generalized isostaticity $Z^m_{iso}(\mu)$ discussed in static packings of frictional spheres [2, 39–42], as shown in Fig. 1. In frictional sphere packings, at a given contact, there are both tangential $f_t$ and normal $f_n$ force components, whose ratio $m \equiv |\frac{f_t}{\mu f_n}|$ satisfies the Coulomb's criterion of $m \leq 1$ with $\mu$ being the frictional coefficient. Fully mobilized Contacts (FMC) are those of $m = 1$ [2, 39–42]. Introducing $n_m$ as the number of FMC per particle, the generalized isostaticity is defined as $Z^m_{iso}(\mu) = d+1+2n_m/d$ [2, 39–42]. The precise determination of $Z^m_{iso}(\mu)$ even in static packings is challenging since $n_m$ depends on preparation protocol [39–42](See also e.g. [50, 51]).

However, it remains open to debate whether $Z^m_{iso}(\mu)$ is the true critical point of frictional packing [39, 41, 42]. It has been shown that if FMC were treated elastically in dynamical matrix the frictional critical point would be at $Z = d + 1$, i.e. the isostaticity of $\mu \to \infty$ [39], where the argument is that tiny perturbations would reset FMC to relax to the almost-fully-mobilized [2, 39]. In contrast, if FMC were treated as free-sliding contacts, the frictional critical point would be at $Z^m_{iso}$ [2, 41].

In our system, $\mu \approx 0.3$, our findings are thus more close to the prediction of Ref. [41] than that of Ref.[39]. Note that at a given FMC, perturbation has an asymmetric effect: if it ('+' perturbation) were applied trying to increase $f_t$ further, the contact would slide; if it ('-' perturbation) were applied oppositely to decrease $f_t$ the contact would be stable with $m < 1$. This asymmetry leads to the breakdown of dynamical matrix and the replacement by Jacobian when treating both '+' and '-' perturbations simultaneously, which predicts a spiral instability [52]. However, we do not observe any clear sign of spiral patterns experimentally. In both Refs [39, 41], the perturbations on a FMC are treated symmetrically so that dynamical matrix can be constructed, except that Ref.[39] permits only '-' perturbation to treat all FMC elastically, whereas Ref.[41] permits only '+' perturbation to treat all FMC as sliding contacts. The strong similarity between our experiment and the prediction of [41] suggests that FMC must have a strong tendency to bias towards '+' perturbation and hence to slide under cyclic shear. Therefore, the system self-organizes to a

critical jamming state through the strong coupling of mechanical structure and dynamics.

Ref.[41] shows that packings prepared using sufficiently gentle protocol approach $Z^m_{iso}(\mu)$ when pressure $p \to 0$, becoming marginally stable [53]. Consequently, the packings show scaling behaviors similar to those of frictionless jamming [1, 4, 41], with two diverging length scales – $l^*$ for longitudinal responses and $l_c$ for transverse responses– governing the break-down of rigidity near jamming [1–4]. We make a rough estimate using $l^* \sim p^{-\frac{1}{2}} \sim 1000$ and $l_c \sim p^{-\frac{1}{4}} \sim 32$ [4], which are consistent with the forementioned experimental results and the two length scales $\xi_L$ and $\xi_T$ discussed from the above.

The contact sliding and the strong coupling between structure and dynamics imply that the frictional packing near critical jamming state is irreversible under cyclic shear regardless of shear strain amplitude, which is confirmed by the monotonic structure relaxation characterized using the self intermediate scattering function (ISF) [54] as shown in Fig. 5, where $k = 5.53$ in ISF corresponding to one mean particle diameter. Results in Fig. 5 differ from those of thermal glasses [55] and frictionless packings, where rich behaviors of reversible-irreversible transition and limit cycles have been observed [24, 56–60]. However, the absence of reversibility here does not preclude the elusive yielding transition [10, 24, 55, 60–64]. Different protocols other than oscillatory shear may be used: for example, using rheological protocol Otsuki et al observed yielding transition in frictional granular packings [65] whereas using oscillatory shear, they did not observe clear distinction in the store and loss moduli [66]. Therefore, it remains open whether yielding transition could be observed experimentally. Lastly, limit cycles and caging are reported in [67]. However, Ref.[67] studies soft-sphere packings with open top surface such that $p$ varies from $p = 0$ at the surface to $p \sim 10^{-2}$ at the bottom. It remains open to what extent the critical frictional jamming would influence strongly heterogeneous systems as studied in Ref.[67].

Applying uniform shear, turbulent-like vortexes were observed numerically in both frictionless [68, 69] and frictional packings [70, 71] as well as in Lenard-Jones glasses [72] since the work of Radjai and coworkers [73], where the physical mechanism is still under heated debate. In energy spectrum $E(k) \propto k^{-\alpha'}$, $\alpha'$ varies from $\alpha' \approx 1.24$ [73], to $\alpha' \approx 1.8$ [70], to $\alpha' \approx 2.0$ [71], to $\alpha' \approx 1.4$ in 2D and $\alpha' \approx 1.5$ in 3D [69], and to $\alpha' \approx 1.3$ [73]. Furthermore, $\alpha'$ varies with packing fraction and shear rate, e.g. in [70]. It remains open the roles the critical frictional jamming might play, but uniformly sheared granular materials have additional complication–single low-frequency-dominant mode couples strongly to shear besides floppy modes [74].

In non-local rheology – stress is not merely determined from local shear rate, different approaches and non-local constitutive relations have been put forwards [75–78].

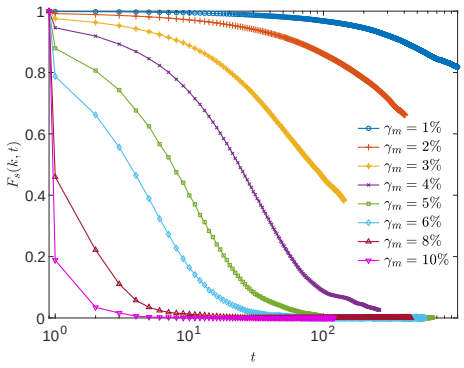


FIG. 5. The self intermediate scattering functions $F_s(k,t)$ of different $\gamma_m$. Here $k = 5.53$ corresponds to one mean particle diameter.

Despite the success [75–78], it is still controversial regarding the microscopic mechanisms. Our findings will help clarify the mechanisms of non-locality at the fundamental level. Our findings may also be relevant to the understanding of the remote triggering in seismology, where a quake happens at one place can trigger another quake at a remote location [79, 80].

To summarize, we have found compelling evidence that frictional hard granular packings under cyclic shear are marginally stable. Our analyses of both spectra of the transverse and longitudinal components and the corresponding temporal spectra show that the system is self-organized near the critical point of jamming with two diverging length scales associated with the transverse and longitudinal modes. These results are consistent with the concept of generalized isostaticity of frictional hard sphere, where contact sliding is crucial for fully mobilized contacts subject to perturbation. Our findings suggest that the concept of jamming is not only relevant but also crucial in determining the dynamical behaviors of real granular materials, which are often composed of frictional and hard particles.

This work is supported by the NSFC (No.11774221 and No.11974238). We also acknowledge the support from the student innovation center of Shanghai Jiao Tong University.

*(jiezhang2012@sjtu.edu.cn)

[1] C. S. O'Hern, L. E. Silbert, A. J. Liu, and S. R. Nagel, Phys Rev E Stat Nonlin Soft Matter Phys **68**, 011306 (2003).
[2] M. van Hecke, J Phys Condens Matter **22**, 033101 (2010).
[3] A. J. Liu and S. R. Nagel, Annual Review of Condensed Matter Physics **1**, 347 (2010).
[4] M. Wyart, L. E. Silbert, S. R. Nagel, and T. A. Witten,

Phys Rev E Stat Nonlin Soft Matter Phys **72**, 051306 (2005).
[5] L. E. Silbert, A. J. Liu, and S. R. Nagel, Physical review letters **95**, 098301 (2005).
[6] W. G. Ellenbroek, E. Somfai, M. van Hecke, and W. van Saarloos, Physical review letters **97**, 258001 (2006).
[7] N. Xu, V. Vitelli, M. Wyart, A. J. Liu, and S. R. Nagel, Physical review letters **102**, 038001 (2009).
[8] D. J. Durian, Phys. Rev. Lett. **75**, 4780 (1995).
[9] C. S. O'Hern, S. A. Langer, A. J. Liu, and S. R. Nagel, Phys. Rev. Lett. **88**, 075507 (2002).
[10] P. Olsson and S. Teitel, Phys Rev Lett **99**, 178001 (2007).
[11] M. Otsuki and H. Hayakawa, Physical Review E **80**, 011308 (2009).
[12] K. N. Nordstrom, E. Verneuil, P. Arratia, A. Basu, Z. Zhang, A. G. Yodh, J. P. Gollub, and D. J. Durian, Physical review letters **105**, 175701 (2010).
[13] B. P. Tighe, E. Woldhuis, J. J. Remmers, W. van Saarloos, and M. van Hecke, Phys Rev Lett **105**, 088303 (2010).
[14] E. DeGiuli, G. Düring, E. Lerner, and M. Wyart, Physical Review E **91**, 062206 (2015).
[15] K. Suzuki and H. Hayakawa, Phys Rev Lett **115**, 098001 (2015).
[16] L. E. Silbert, A. J. Liu, and S. R. Nagel, Physical Review E **73**, 041304 (2006).
[17] P. Charbonneau, J. Kurchan, G. Parisi, P. Urbani, and F. Zamponi, Nature communications **5**, 1 (2014).
[18] P. Charbonneau, E. I. Corwin, G. Parisi, and F. Zamponi, Physical review letters **109**, 205501 (2012).
[19] M. Wyart, Physical review letters **109**, 125502 (2012).
[20] E. Lerner, G. Düring, and M. Wyart, Soft Matter **9**, 8252 (2013).
[21] C. Heussinger and J.-L. Barrat, Physical review letters **102**, 218303 (2009).
[22] H. A. Vinutha and S. Sastry, Nature Physics **12**, 578 (2016).
[23] P. Urbani and F. Zamponi, Phys Rev Lett **118**, 038001 (2017).
[24] Y. Jin, P. Urbani, F. Zamponi, and H. Yoshino, Science Advances **4**, eaat6387 (2018).
[25] K. Baumgarten, D. Vagberg, and B. P. Tighe, Phys Rev Lett **118**, 098001 (2017).
[26] S. F. Edwards and R. Oakeshott, Physica A: Statistical Mechanics and its Applications **157**, 1080 (1989).
[27] S. Henkes, C. S. O'Hern, and B. Chakraborty, Phys Rev Lett **99**, 038002 (2007).
[28] C. Song, P. Wang, and H. A. Makse, Nature **453**, 629 (2008).
[29] S. Martiniani, K. J. Schrenk, K. Ramola, B. Chakraborty, and D. Frenkel, Nature Physics **13**, 848 (2017).
[30] R. C. Ball and R. Blumenfeld, Phys. Rev. Lett. **88**, 115505 (2002).
[31] R. Blumenfeld and S. F. Edwards, J Phys Chem B **113**, 3981 (2009).
[32] D. Bi, S. Henkes, K. E. Daniels, and B. Chakraborty, Annu. Rev. Condens. Matter Phys. **6**, 63 (2015).
[33] S. Henkes and B. Chakraborty, Phys. Rev. E **79**, 061301 (2009).
[34] A. Baule, F. Morone, H. J. Herrmann, and H. A. Makse, Reviews of Modern Physics **90** (2018), 10.1103/RevModPhys.90.015006.
[35] J. H. Snoeijer, T. J. Vlugt, M. van Hecke, and W. van Saarloos, Physical review letters **92**, 054302 (2004).
[36] B. P. Tighe, A. R. T. van Eerd, and T. J. H. Vlugt, Phys. Rev. Lett. **100**, 238001 (2008).
[37] B. P. Tighe and T. J. Vlugt, Journal of Statistical Mechanics: Theory and Experiment **2011**, P04002 (2011).
[38] P. Charbonneau, J. Kurchan, G. Parisi, P. Urbani, and F. Zamponi, Annual Review of Condensed Matter Physics **8**, 265 (2017).
[39] E. Somfai, M. van Hecke, W. G. Ellenbroek, K. Shundyak, and W. van Saarloos, Phys Rev E Stat Nonlin Soft Matter Phys **75**, 020301 (2007).
[40] L. E. Silbert, Soft Matter **6** (2010), 10.1039/c001973a.
[41] S. Henkes, M. van Hecke, and W. van Saarloos, EPL (Europhysics Letters) **90** (2010), 10.1209/0295-5075/90/14003.
[42] K. Shundyak, M. van Hecke, and W. van Saarloos, Phys Rev E Stat Nonlin Soft Matter Phys **75**, 010301 (2007).
[43] S. Henkes, K. Kostanjevec, J. M. Collinson, R. Sknepnek, and E. Bertin, Nat Commun **11**, 1405 (2020).
[44] J. Zheng, A. Sun, Y. Wang, and J. Zhang, Phys Rev Lett **121**, 248001 (2018).
[45] J. E. Thomas, K. Ramola, A. Singh, R. Mari, J. F. Morris, and B. Chakraborty, Phys Rev Lett **121**, 128002 (2018).
[46] J. N. Nampoothiri, Y. Wang, K. Ramola, J. Zhang, S. Bhattacharjee, and B. Chakraborty, Phys Rev Lett **125**, 118002 (2020).
[47] E. DeGiuli, Phys Rev Lett **121**, 118001 (2018).
[48] Y. Wang, Y. Wang, and J. Zhang, Nat Commun **11**, 4349 (2020).
[49] A. Lemaitre, Phys Rev E **96**, 052101 (2017).
[50] T. Unger, J. Kertesz, and D. E. Wolf, Phys Rev Lett **94**, 178001 (2005).
[51] S. Papanikolaou, C. S. O'Hern, and M. D. Shattuck, Phys Rev Lett **110**, 198002 (2013).
[52] J. Chattoraj, O. Gendelman, M. Pica Ciamarra, and I. Procaccia, Phys Rev Lett **123**, 098003 (2019).
[53] M. Müller and M. Wyart, Annual Review of Condensed Matter Physics **6**, 177 (2015).
[54] L. Berthier and G. Biroli, Reviews of Modern Physics **83**, 587 (2011).
[55] P. Leishangthem, A. D. Parmar, and S. Sastry, Nat Commun **8**, 14653 (2017).
[56] D. Fiocco, G. Foffi, and S. Sastry, Phys Rev E Stat Nonlin Soft Matter Phys **88**, 020301 (2013).
[57] I. Regev, T. Lookman, and C. Reichhardt, Phys Rev E Stat Nonlin Soft Matter Phys **88**, 062401 (2013).
[58] I. Regev, J. Weber, C. Reichhardt, K. A. Dahmen, and T. Lookman, Nat Commun **6**, 8805 (2015).
[59] M. O. Lavrentovich, A. J. Liu, and S. R. Nagel, Phys Rev E **96**, 020101 (2017).
[60] S. Dagois-Bohy, E. Somfai, B. P. Tighe, and M. van Hecke, Soft Matter **13**, 9036 (2017).
[61] G. Parisi, I. Procaccia, C. Rainone, and M. Singh, Proc Natl Acad Sci U S A **114**, 5577 (2017).
[62] P. K. Jaiswal, I. Procaccia, C. Rainone, and M. Singh, Phys Rev Lett **116**, 085501 (2016).
[63] A. Ikeda, L. Berthier, and P. Sollich, Phys Rev Lett **109**, 018301 (2012).
[64] P. Olsson and S. Teitel, Phys Rev Lett **109**, 108001 (2012).
[65] M. Otsuki and H. Hayakawa, Phys Rev E Stat Nonlin Soft Matter Phys **83**, 051301 (2011).
[66] M. Otsuki and H. Hayakawa, Phys Rev E **101**, 032905 (2020).

[67] J. R. Royer and P. M. Chaikin, Proc Natl Acad Sci U S A **112**, 49 (2015).
[68] D. Vagberg, P. Olsson, and S. Teitel, Phys Rev Lett **113**, 148002 (2014).
[69] N. Oyama, H. Mizuno, and K. Saitoh, Phys Rev Lett **122**, 188004 (2019).
[70] K. Saitoh and H. Mizuno, Soft Matter **12**, 1360 (2016).
[71] K. Saitoh and H. Mizuno, Phys Rev E **94**, 022908 (2016).
[72] C. Goldenberg, A. Tanguy, and J. L. Barrat, Europhysics Letters (EPL) **80** (2007), 10.1209/0295-5075/80/16003.
[73] F. Radjai and S. Roux, Phys Rev Lett **89**, 064302 (2002).
[74] E. Lerner, G. During, and M. Wyart, Proc Natl Acad Sci U S A **109**, 4798 (2012).
[75] K. Kamrin and G. Koval, Phys Rev Lett **108**, 178301 (2012).
[76] M. Bouzid, M. Trulsson, P. Claudin, E. Clement, and B. Andreotti, Phys Rev Lett **111**, 238301 (2013).
[77] D. L. Henann and K. Kamrin, Proc Natl Acad Sci U S A **110**, 6730 (2013).
[78] M. Bouzid, A. Izzet, M. Trulsson, E. Clement, P. Claudin, and B. Andreotti, Eur Phys J E Soft Matter **38**, 125 (2015).
[79] E. E. Brodsky, V. Karakostas, and H. Kanamori, Geophysical Research Letters **27**, 2741 (2000).
[80] J. E. Elkhoury, E. E. Brodsky, and D. C. Agnew, Nature **441**, 1135 (2006).

## SUPPLEMENTARY MATERIALS

In the Supplementary Materials, we provide additional information on: (1) the definitions of velocity power spectrum in $k$ space and $\omega$ domain, (2) the theoretical model originally developed by S. Henkes and coworkers [43], (3) the probability distribution functions of velocity.

**1. The definitions of velocity power spectrum in $k$ space and $\omega$ domain**

**1.1. The definition of spectrum in $k$ space**

We use $\mathbf{v}_i$ with $i = 1, ...N$ to represent velocity field of all $N$ particles at $\gamma = 0$, with $\gamma$ refering to the axial strain within a shear cycle ($\gamma = 0$ represents the symmetric middle point of axial strain within a shear cycle). Here, $\mathbf{v}_i$ refers to particle displacement at $\gamma = 0$ between two shear cycles of $t$ and $t + 1$: $\mathbf{v}_i(t, \gamma = 0) \equiv \mathbf{r}_i(t + 1, \gamma = 0) - \mathbf{r}_i(t, \gamma = 0)$ where $\mathbf{r}_i(t, \gamma)$ is the potition of particle $i$ at a given strain $\gamma$ within a shear cycle $t$. For simplicity, we use $\mathbf{v}_i$ for $\mathbf{v}_i(t, \gamma = 0)$ and, likewise, $\mathbf{r}_i$ for $\mathbf{r}_i(t, \gamma = 0)$ in the following definitions in sections **1.1** and **1.2**.

We decompose $\mathbf{v}_i$ into the longitudinal and transverse components and define the longitudinal (L) and transverse (T) spectra as:

$$E_L(\mathbf{k}) = \frac{\rho_0}{2} \left\langle \frac{1}{N} \left| \sum_i^N \mathbf{v}_{i,\parallel} e^{-j\mathbf{k}\cdot\mathbf{r}_i} \right|^2 \right\rangle, \tag{2}$$

and

$$E_T(\mathbf{k}) = \frac{\rho_0}{2} \left\langle \frac{1}{N} \left| \sum_i^N \mathbf{v}_{i,\perp} e^{-j\mathbf{k}\cdot\mathbf{r}_i} \right|^2 \right\rangle, \tag{3}$$

respectively. Here, $j \equiv \sqrt{-1}$, $\rho_0 = N/L^2$, with $L$ being the system size, is the particle number density, and $\mathbf{v}_{i,\parallel}$ and $\mathbf{v}_{i,\perp}$ are the components parallel and perpendicular to wavenumber vector $\mathbf{k}$, respectively. Furthermore, $\mathbf{v}_{i,\parallel} \equiv (\mathbf{v}_i \cdot \hat{\mathbf{k}})\hat{\mathbf{k}}$ with $\hat{\mathbf{k}}$ being the unit wavenumber vector, and $\mathbf{v}_{i,\perp} \equiv \mathbf{v}_i - \mathbf{v}_{i,\parallel}$. The angular brackets represent ensemble and time average in steady state. For $\gamma_m < 5\%$, we average more than three independent experimental runs.

**1.2. the definition of spectrum in $\omega$ domain**

Here, $E(\omega)$ is defined as follow,

$$E(\omega) = \left\langle \frac{1}{N} \sum_{i=1}^{N} \frac{1}{T} \left| \sum_{t=0}^{T} \mathbf{v}_i e^{-j\omega t} \right|^2 \right\rangle, \tag{4}$$

where $T$ is the number of shear cycles in steady state.

**2. The theoretical model of S. Henkes and coworkers**

**2.1. The main equation of the model**

To understand the spectra in Fig.3 and Fig.4 in the main text, we first introduce a phenomenological model originally developed by Henkes et. al. in the context of describing the motion pattern of active matter [43]. There are several slightly different formulations of their model, but we will only introduce their continuum elastic formulation since it is simple and intuitive. The main equation of the continuum formulation is

$$\zeta \dot{\mathbf{u}} = \zeta v_0 \hat{\mathbf{n}} + \bigtriangledown \cdot \hat{\sigma}, \tag{5}$$

where $\mathbf{u}$ is the displacement at a given position and time, $\zeta$ is a drag coefficient, the first term on the right-hand side ($r.h.s$) represents a noise term with a mean strength $v_0$ and random orientation $\hat{\mathbf{n}}$ [43], and the second term on $r.h.s$ represents force from a continuous elastic field. In the case of granular material, we can think the first term on $r.h.s$ as a simplified model of the particle-particle interaction due to random fluctuations of unbalanced contact forces by neglecting its spatial structure and we can think this second term on $r.h.s$ as a mean-field-type effective elastic field, which is consistent with the stress theories of amorphous materials [45–47, 49] and the recent experimental verification [48].

**2.2. Velocity power spectra in the wavenumber space**

Assumming linear elasticity with bulk and shear moduli $B$ and $\mu$, respectively, eq.5 becomes

$$\zeta \dot{\mathbf{u}} = \zeta v_0 \hat{\mathbf{n}} + B \bigtriangledown (\bigtriangledown \cdot \mathbf{u}) + \mu \bigtriangleup \mathbf{u}. \tag{6}$$

In Fourier $\mathbf{q}$ space, eq.6 becomes

$$\zeta \dot{\tilde{\mathbf{u}}} = \mathbf{F}(\mathbf{q}, t) - D(\mathbf{q})\tilde{\mathbf{u}}, \tag{7}$$

where

$$\mathbf{F}(\mathbf{q}, t) \equiv \zeta v_0 \int \hat{\mathbf{n}}(\mathbf{r}, t) e^{i\mathbf{q}\cdot\mathbf{r}} d^2\mathbf{r}, \tag{8}$$

$$\tilde{\mathbf{u}}(\mathbf{q},t) \equiv \int \mathbf{u}(\mathbf{r},t) e^{i\mathbf{q}\cdot\mathbf{r}} d^2\mathbf{r}, \tag{9}$$

and the dynamical matrix $D(\mathbf{q})$ is defined as

$$D(\mathbf{q}) = \begin{bmatrix} Bq_x^2 + \mu q^2 & Bq_x q_y \\ Bq_y q_x & Bq_y^2 + \mu q^2 \end{bmatrix}, \tag{10}$$

in which $q_x \equiv \mathbf{q}\cdot\hat{x}$, $q_y \equiv \mathbf{q}\cdot\hat{y}$, $q \equiv |\mathbf{q}|$. The diagnolization of $D(\mathbf{q})$ yields two modes in two dimensions, i.e. the longitudinal mode ($L$) with the corresponding wave vector $\hat{\mathbf{q}}$ and the transverse mode ($T$) with the corresponding wave vector $\mathbf{q}^\perp$. By decomposing eq. 7 into the $L$ and $T$ components, one obtains two corresponding equations

$$\begin{aligned} \zeta \dot{\tilde{u}}_L &= -(B+\mu) q^2 \tilde{u}_L + F_L(\mathbf{q},t), \\ \zeta \dot{\tilde{u}}_T &= -\mu q^2 \tilde{u}_T + F_T(\mathbf{q},t), \end{aligned} \tag{11}$$

where

$$\begin{aligned} F_L(\mathbf{q},t) &\equiv \mathbf{F}(\mathbf{q},t)\cdot\hat{\mathbf{q}}, \\ F_T(\mathbf{q},t) &\equiv \mathbf{F}(\mathbf{q},t)\cdot\mathbf{q}^\perp, \\ \tilde{u}_L &\equiv \tilde{\mathbf{u}}\cdot\hat{\mathbf{q}}, \\ \tilde{u}_T &\equiv \tilde{\mathbf{u}}\cdot\mathbf{q}^\perp, \\ \hat{\mathbf{q}} &\equiv \mathbf{q}/q, \\ \mathbf{q}^\perp &\equiv (q_y\hat{x} - q_x\hat{y})/q. \end{aligned} \tag{12}$$

One then applies a time Fourier transform for eq. 11 and obtains

$$\begin{aligned} i\zeta\omega\tilde{u}_L(\mathbf{q},\omega) &= -(B+\mu)q^2\tilde{u}_L(\mathbf{q},\omega) + F_L(\mathbf{q},\omega), \\ i\zeta\omega\tilde{u}_T(\mathbf{q},\omega) &= -\mu q^2\tilde{u}_T(\mathbf{q},\omega) + F_T(\mathbf{q},\omega). \end{aligned} \tag{13}$$

Note that in Henkes et al's orginal paper [43], the '$-$' sign on the left hand side of their eq.(44) in the Supplemetary Materials of Ref.[43] seems to be '+' instead. But this sign change is not going to affect their spectrum results since all $\omega$ appears in the quadratic form $\omega^2$ Ref.[43]. In the above eq. 13, the time Fourier transforms are defined as

$$\begin{aligned} F_L(\mathbf{q},\omega) &\equiv \int F_L(\mathbf{q},t) e^{i\omega t} dt, \\ F_T(\mathbf{q},\omega) &\equiv \int F_T(\mathbf{q},t) e^{i\omega t} dt, \\ \tilde{u}_L(\mathbf{q},\omega) &\equiv \int \tilde{u}_L(\mathbf{q},t) e^{i\omega t} dt, \\ \tilde{u}_T(\mathbf{q},\omega) &\equiv \int \tilde{u}_T(\mathbf{q},t) e^{i\omega t} dt. \end{aligned} \tag{14}$$

Next let us define velocity and its $L$ and $T$ components as

$$\begin{aligned} \tilde{\mathbf{v}}(\mathbf{q},\omega) &\equiv i\omega\tilde{\mathbf{u}}(\mathbf{q},\omega), \\ \tilde{v}_L(\mathbf{q},\omega) &\equiv i\omega\tilde{u}_L(\mathbf{q},\omega), \\ \tilde{v}_T(\mathbf{q},\omega) &\equiv i\omega\tilde{u}_T(\mathbf{q},\omega). \end{aligned} \tag{15}$$

.

Using eq. 13, one can find the ensemble averaged spectra of the $L$ and $T$ modes

$$\begin{aligned} &\langle \tilde{v}_L(\mathbf{q},t)\tilde{v}_L(\mathbf{q}',t)\rangle = \\ &\frac{1}{(2\pi)^2}\int d\omega \int d\omega' e^{-i(\omega+\omega')t}\langle \tilde{v}_L(\mathbf{q},\omega)\tilde{v}_L(\mathbf{q}',\omega')\rangle \\ &= \frac{2\pi^2 a^2 \zeta \upsilon_0^2}{(B+\mu)\tau q^2 + \zeta}\delta(\mathbf{q}+\mathbf{q}'), \end{aligned} \tag{16}$$

and

$$\begin{aligned} &\langle \tilde{v}_T(\mathbf{q},t)\tilde{v}_T(\mathbf{q}',t)\rangle = \\ &\frac{1}{(2\pi)^2}\int d\omega \int d\omega' e^{-i(\omega+\omega')t}\langle \tilde{v}_T(\mathbf{q},\omega)\tilde{v}_T(\mathbf{q}',\omega')\rangle \\ &= \frac{2\pi^2 a^2 \zeta \upsilon_0^2}{\mu\tau q^2 + \zeta}\delta(\mathbf{q}+\mathbf{q}'). \end{aligned} \tag{17}$$

Note that in order to compute the two terms of $\langle \tilde{v}_L(\mathbf{q},\omega)\tilde{v}_L(\mathbf{q}',\omega')\rangle$ and $\langle \tilde{v}_T(\mathbf{q},\omega)\tilde{v}_T(\mathbf{q}',\omega')\rangle$ in eq. 16 and eq. 17 from eq. 13, it is implicitly assumed that the spatial and temporal correlation function of the stochastic random orientation unit vector $\hat{\mathbf{n}}$ in eq. 5 and eq. 6 must satisfy the following form

$$\langle \hat{\mathbf{n}}(\mathbf{r},t)\cdot\hat{\mathbf{n}}(\mathbf{r}',t')\rangle = a^2\delta(\mathbf{r}-\mathbf{r}')e^{-|t-t'|/\tau}. \tag{18}$$

From eq. 18, it can be shown that

$$\begin{aligned} \langle \mathbf{F}(\mathbf{q},\omega)\cdot\mathbf{F}(\mathbf{q}',\omega')\rangle &= \zeta^2\upsilon_0^2\int_{-\infty}^{\infty} dt \int_{-\infty}^{\infty} dt' \int d^2\mathbf{r} \int d^2\mathbf{r}' \\ &e^{i\omega t} e^{i\mathbf{q}\cdot\mathbf{r}} e^{i\omega' t'} e^{i\mathbf{q}'\cdot\mathbf{r}'} \langle \hat{\mathbf{n}}(\mathbf{r},t)\cdot\hat{\mathbf{n}}(\mathbf{r}',t')\rangle \\ &= (2\pi)^3 a^2\zeta^2\upsilon_0^2 \frac{2\tau}{1+(\tau\omega)^2}\delta(\mathbf{q}+\mathbf{q}')\delta(\omega+\omega'). \end{aligned} \tag{19}$$

Using eq. 17 and together with the fact that

$$\begin{aligned} \langle F_L(\mathbf{q},\omega)F_L(\mathbf{q}',\omega')\rangle &= \langle F_T(\mathbf{q},\omega)F_T(\mathbf{q}',\omega')\rangle \\ &= \frac{1}{2}\langle \mathbf{F}(\mathbf{q},\omega)\cdot\mathbf{F}(\mathbf{q}',\omega')\rangle, \end{aligned} \tag{20}$$

it yields

$$\begin{aligned} &\langle \tilde{v}_L(\mathbf{q},\omega)\tilde{v}_L(\mathbf{q}',\omega')\rangle \\ &= \frac{(2\pi)^3 a^2\zeta^2\upsilon_0^2\tau\omega^2}{[(B+\mu)^2q^4 + \zeta^2\omega^2][1+(\tau\omega)^2]}\delta(\mathbf{q}+\mathbf{q}')\delta(\omega+\omega'), \end{aligned} \tag{21}$$

and

$$\begin{aligned} &\langle \tilde{v}_T(\mathbf{q},\omega)\tilde{v}_T(\mathbf{q}',\omega')\rangle \\ &= \frac{(2\pi)^3 a^2\zeta^2\upsilon_0^2\tau\omega^2}{[\mu^2q^4 + \zeta^2\omega^2][1+(\tau\omega)^2]}\delta(\mathbf{q}+\mathbf{q}')\delta(\omega+\omega'), \end{aligned} \tag{22}$$

which supplement the missing details in the derivation of eq. 16 and eq. 17. The eq. 16 and eq. 17 can be written

in more compact form as

$$\langle \tilde{v}_L(\mathbf{q},t)\tilde{v}_L(\mathbf{q}',t')\rangle = 2\pi^2 a^2 v_0^2 \frac{1}{1+(\xi_L q)^2}\delta(\mathbf{q}+\mathbf{q}'),$$
$$\langle \tilde{v}_T(\mathbf{q},t)\tilde{v}_T(\mathbf{q}',t')\rangle = 2\pi^2 a^2 v_0^2 \frac{1}{1+(\xi_T q)^2}\delta(\mathbf{q}+\mathbf{q}'), \tag{23}$$

where

$$\xi_L \equiv \sqrt{\frac{(B+\mu)\tau}{\zeta}}, \qquad \xi_T \equiv \sqrt{\frac{\mu\tau}{\zeta}}, \tag{24}$$

are the longitudinal and transverse correlation lengths, respectively. In discrete case, the Dirac delta function becomes Kronecker delta,

$$\delta(\mathbf{q}+\mathbf{q}') \to \frac{1}{(\triangle q)^2}\delta_{\mathbf{-q},\mathbf{q}'}, \tag{25}$$

with $\triangle q \equiv \frac{2\pi}{L}$, and $L$ being the system size. Furthermore, we have

$$\int d^2\mathbf{r} \to a^2 \Sigma_{\mathbf{r}}, \tag{26}$$

which introduces a factor of $\frac{1}{a^2}$ when converting the continuous $\tilde{\mathbf{v}}(\mathbf{q},t)$ to the discrete version

$$\mathbf{v}(\mathbf{q},t) = \frac{1}{a^2}\tilde{\mathbf{v}}(\mathbf{q},t). \tag{27}$$

Finally, we obtain the spetra in discrete case using $N = L^2/a^2$,

$$\langle v_L(\mathbf{q},t)v_L(-\mathbf{q},t)\rangle = \frac{N}{2}v_0^2\frac{1}{1+(\xi_L q)^2} \to \frac{N v_0^2}{2\xi_L^2 q^2} \propto \frac{1}{q^2}, \tag{28}$$

when $\xi_L \geq \frac{L}{2}$, and

$$\langle v_T(\mathbf{q},t)v_T(-\mathbf{q},t)\rangle = \frac{N}{2}v_0^2\frac{1}{1+(\xi_T q)^2} \to \frac{N v_0^2}{2\xi_T^2 q^2} \propto \frac{1}{q^2}, \tag{29}$$

when $\xi_T \geq \frac{L}{2}$. Note that in Ref.[43], the wave number vector and its corresponding modulus are represented using notation $\mathbf{q}$ and $q$, whereas in this paper, we use $\mathbf{k}$ and $k$ instead. Finally, we have, in our notation

$$E_L(k) = \langle v_L(\mathbf{k},t)v_L(-\mathbf{k},t)\rangle \propto \frac{1}{k^2}, \tag{30}$$

when $\xi_L \geq \frac{L}{2}$, and

$$E_T(k) = \langle v_T(\mathbf{k},t)v_T(-\mathbf{k},t)\rangle \propto \frac{1}{k^2}, \tag{31}$$

when $\xi_T \geq \frac{L}{2}$.

The tremendous insight from the above simple phenomenological model is that the velocity power spectra $\propto k^{-2}$ shown in Fig.3 in the main text can be reproduced as a consequence of two key characteristics: (1) the presence of an effective elastic medium with stochastic random forcing between particles; (2) diverging correlation length scales. The first characteristic implies that system must be jammed, and the second one then implies that the system must be near its critical point of jamming. The agreement between the results in Fig.3 in the main text and the predictions of eq. 30 and eq. 31 is remarkable considering that frictional granular materials of spheres in 3D and circles in 2D are generally hyperstatic in nature [2, 3].

**Remark** Here we will discuss more about the notation of Fourier transform and inverse Fourier transform introduced in Ref.[43], as already introduced from the above. In conventional notation of Fourier transform from a function $f(x)$ to $F(k)$, it is usually written as

$$F(k) = \int f(x)e^{-ikx}dx, \tag{32}$$

and correspondingly, the inverse transform is written as

$$f(x) = \frac{1}{2\pi}\int F(x)e^{ikx}dk. \tag{33}$$

In Ref.[SHenkes NC 2020], they use instead

$$F(k) = \int f(x)e^{ikx}dx, \tag{34}$$

and correspondingly, the inverse transform is written as

$$f(x) = \frac{1}{2\pi}\int F(x)e^{-ikx}dk, \tag{35}$$

as shown here in eq. 8, eq. 9, eq. 14, and eq. 19. Therefore, there is a minus sign difference in the exponential function compared to the conventional notation. However, this difference will not change their derived equations in any significant way as long as one is aware of that.

### 2.3. Velocity power spectra in angular frequency domain

In the following, we will derive the energy spectra of velocity fluctuations in angular frequency domain. First, we will use $\xi$ to represent either $\xi_L$ or $\xi_T$ by omitting the subscript $L$ or $T$ for simplicity, unless otherwise stated.

From eq. 21 and eq. 22, we will get

$$\begin{aligned}
&\langle\tilde{v}(\mathbf{q},\omega)\tilde{v}(\mathbf{q}',\omega')\rangle \\
&= \frac{(2\pi)^3 a^2 v_0^2 \tau\omega^2}{[\frac{(\xi q)^4}{\tau^2}+\omega^2][1+(\tau\omega)^2]}\delta(\mathbf{q}+\mathbf{q}')\delta(\omega+\omega') \\
&= \frac{(2\pi)^3 a^2 v_0^2 \tau}{1+(\tau\omega)^2}\frac{\tau^2\omega^2}{(\xi q)^4+(\tau\omega)^2}\delta(\mathbf{q}+\mathbf{q}')\delta(\omega+\omega') \\
&= \frac{(2\pi)^3 a^2 v_0^2 \tau}{1+(\tau\omega)^2}\phi(\mathbf{q},\mathbf{q}',\omega)\delta(\omega+\omega'),
\end{aligned} \tag{36}$$

where we have defined

$$\phi(\mathbf{q},\mathbf{q}',\omega) \equiv \frac{\tau^2\omega^2}{(\xi q)^4+(\tau\omega)^2}\delta(\mathbf{q}+\mathbf{q}'). \tag{37}$$

To compute spectrum in angular frequency domain, we need to integrate $\mathbf{q}$ and $\mathbf{q}'$ for eq. 36 and hence eq. 37. The integration of eq. 37 in the $\mathbf{q}$ and $\mathbf{q}'$ space gives

$$\begin{aligned}
&\int\int \phi(\mathbf{q},\mathbf{q}',\omega)d^2\mathbf{q}d^2\mathbf{q}' \\
&= \int\int \frac{\tau^2\omega^2}{(\xi q)^4+(\tau\omega)^2}\delta(\mathbf{q}+\mathbf{q}')d^2\mathbf{q}d^2\mathbf{q}' \\
&= \frac{1}{(\Delta q)^2}\int \frac{(\tau\omega)^2}{(\xi q)^4+(\tau\omega)^2}d^2\mathbf{q},
\end{aligned} \tag{38}$$

where we have applied eq. 25 in the last step of derivation. Next, we let $\Omega \equiv \tau\omega$ and $Q \equiv \xi q$. Note that $d^2\mathbf{q} = \frac{\pi}{\xi^2}dQ^2$. We then get

$$\begin{aligned}
&\int\int \phi(\mathbf{q},\mathbf{q}',\omega)d^2\mathbf{q}d^2\mathbf{q}' \\
&= \frac{\pi}{(\Delta q)^2\xi^2}\int \frac{\Omega^2}{Q^4+\Omega^2}dQ^2 \\
&= \frac{\pi\Omega^2}{(\Delta q)^2\xi^2}\int \frac{1}{Q'^2+\Omega^2}dQ',
\end{aligned} \tag{39}$$

with $Q' \equiv Q^2$. To compute the integration in eq. 39, we need to specify the upper and lower bounds $\alpha_c$ and $\alpha_f$, respectively. First, it is easy to see that the upper bound $\alpha_c$ can essentially be replaced by infinity. This is because $\alpha_c = (\xi 2\pi/l_o)^2 = (\xi 2\pi)^2 \to \infty$, where $l_o$ refers to the particle size and $l_o = 1$ in the units of small particle diameter. Second, it is also easy to show that the lower bound $\alpha_f$ is much larger than one. This is because $\alpha_f = (\xi 2\pi/L)^2 \gg 1$ if $\xi \geq \frac{L}{2}$, which is true in our system. Now we are ready to compute the integral in eq. 39 as shown below

$$\begin{aligned}
\int_{\alpha_f}^{\alpha_c}\frac{1}{Q'^2+\Omega^2}dQ' &= \int_{\alpha_f}^{\infty}\frac{1}{Q'^2+\Omega^2}dQ' \\
&= \frac{1}{\Omega}\,tan^{-1}\big(\frac{Q'}{\Omega}\big)\Big|_{\alpha_f}^{\infty} \\
&= \frac{1}{\Omega}\Big(\frac{\pi}{2}-tan^{-1}(\frac{\alpha_f}{\Omega})\Big) = \frac{1}{\Omega}tan^{-1}(\frac{\Omega}{\alpha_f}),
\end{aligned} \tag{40}$$

where we have applied a mathematical relation $tan^{-1}(\frac{1}{x}) = \frac{\pi}{2} - tan^{-1}(x)$. Since our experiment is subject to quasi-static cyclic shear, $\omega$ is presumably sufficiently slow such that

$$\frac{Q'}{\Omega} = \frac{Q^2}{\Omega} = \frac{\xi^2 q^2}{\Omega} = \frac{C\tau q^2}{\zeta\tau\omega} = \frac{Cq^2}{\zeta\omega} \gg 1, \tag{41}$$

with $C = B + \mu$ for longitudinal mode and $C = \mu$ for transverse mode, and $Q' \geq \alpha_f$. Moreover, we apply the mathematical relation $tan^{-1}(x) = x$, when $|x| \ll 1$, which leads to

$$\int_{\alpha_f}^{\alpha_c}\frac{1}{Q'^2+\Omega^2}dQ' = \frac{1}{\alpha_f}. \tag{42}$$

Hence, eq. 39 becomes

$$\begin{aligned}
&\int\int \phi(\mathbf{q},\mathbf{q}',\omega)d^2\mathbf{q}d^2\mathbf{q}' \\
&= \frac{\pi\Omega^2}{(\Delta q)^2\xi^2\alpha_f} = \frac{\pi(\tau\omega)^2}{(\Delta q)^4\xi^4}.
\end{aligned} \tag{43}$$

Finally, we can compute the spectrum $E(\omega)$ in angular frequency domain through

$$\begin{aligned}
E(\omega)\delta(\omega+\omega') &\equiv \int\int\langle\tilde{v}(\mathbf{q},\omega)\tilde{v}(\mathbf{q}',\omega')\rangle d^2\mathbf{q}d^2\mathbf{q}' \\
&= \int\int \frac{(2\pi)^3 a^2 v_0^2\tau}{1+(\tau\omega)^2}\phi(\mathbf{q},\mathbf{q}',\omega)\delta(\omega+\omega')d^2\mathbf{q}d^2\mathbf{q}' \\
&= \frac{(2\pi)^3 a^2 v_0^2\tau}{1+(\tau\omega)^2}\frac{\pi(\tau\omega)^2}{(\Delta q)^4\xi^4}\delta(\omega+\omega') \\
&= \frac{8\pi^4 a^2 v_0^2\tau}{(\Delta q)^4\xi^4}\delta(\omega+\omega'),
\end{aligned} \tag{44}$$

where the last step is due to $(\tau\omega)^2 \gg 1$ for nonequilibrium systems, as discussed in Ref.[43]. The above equation suggests that the spectrum

$$E(\omega) = \frac{8\pi^4 a^2 v_0^2\tau}{(\Delta q)^4\xi^4} = const., \tag{45}$$

independent of $\omega$.

**3. The PDFs of velocity**

The PDFs of velocity component show collapse onto a single curve once properly normalized, as shown in SFig. S1.

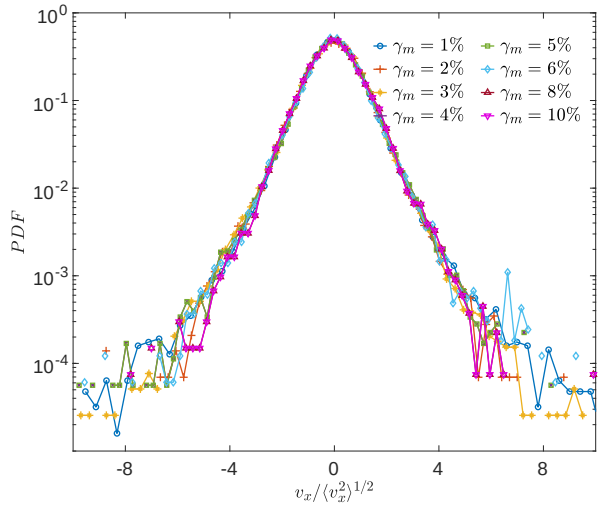


Figure S1. The probability distribution functions (PDFs) of the $x$ component of velocity. Each PDF curve is scaled by the corresponding standard deviation. Note that the results of the $y$ component (not shown) are similar.